AGU PUBLICATIONS

JGR

Journal of Geophysical Research: Oceans

RESEARCH ARTICLE

10.1002/2016JC012431

Special Section:

Atmosphere-ice-ocean-ecosystem Processes in a Thinner Arctic Sea Ice Regime: the Norwegian Young Sea ICE Cruise 2015 (N-ICE2015)

One-dimensional evolution of the upper water column in the Atlantic sector of the Arctic Ocean in winter

Ilker Fer[1], Algot K. Peterson[1], Achim Randelhoff[2,3], and Amelie Meyer[3]

[1]Geophysical Institute, University of Bergen and Bjerknes Centre for Climate Research, Bergen, Norway, [2]Institute for Arctic and Marine Biology, UiT The Arctic University of Norway, Tromsø, Norway, [3]Norwegian Polar Institute, Fram Centre, Tromsø, Norway

Abstract A one-dimensional model is employed to reproduce the observed time evolution of hydrographic properties in the upper water column during winter, between 26 January and 11 March 2015, in a region north of Svalbard in the Nansen Basin of the Arctic Ocean. From an observed initial state, vertical diffusion equations for temperature and salinity give the hydrographic conditions at a later stage. Observations of microstructure are used to synthesize profiles of vertical diffusivity, *K*, representative of varying wind forcing conditions. The ice-ocean heat and salt fluxes at the ice-ocean interface are implemented as external source terms, estimated from the salt and enthalpy budgets, using friction velocity from the Rossby similarity drag relation, and the ice core temperature profiles. We are able to reproduce the temporal evolution of hydrography satisfactorily for two pairs of measured profiles, suggesting that the vertical processes dominated the observed changes. Sensitivity tests reveal a significant dependence on *K*. Variation in other variables, such as the temperature gradient of the sea ice, the fraction of heat going to ice melt, and the turbulent exchange coefficient for heat, are relatively less important. The increase in salinity as a result of freezing and brine release is approximately 10%, significantly less than that due to entrainment (90%) from beneath the mixed layer. Entrainment was elevated during episodic storm events, leading to melting. The results highlight the contribution of storms to mixing in the upper Arctic Ocean and its impact on ice melt and mixed-layer salt and nutrient budgets.

Key Points:
- A 1-D model captures the upper 200 m hydrographic variability in winter in Nansen Basin, north of Svalbard
- Melting occurs in response to entrainment during episodic strong wind forcing
- Increase in mixed-layer salinity from freezing (10%) is significantly less than that due to entrainment (90%)

Correspondence to:
I. Fer,
ilker.fer@uib.no

Citation:
Fer, I., A. K. Peterson, A. Randelhoff, and A. Meyer (2017), One-dimensional evolution of the upper water column in the Atlantic sector of the Arctic Ocean in winter, *J. Geophys. Res. Oceans*, *122*, doi:10.1002/2016JC012431.

Received 5 OCT 2016
Accepted 15 JAN 2017
Accepted article online 11 FEB 2017

1. Introduction

Below an upper surface layer with temperature near its freezing point, the Arctic Ocean water column warms toward subsurface waters of Atlantic origin [*Carmack et al*., 2015; *Rudels*, 2015]. The heat content of the relatively warm layer can affect the presence and evolution of the sea ice cover provided that mixing processes acting along or across density surfaces allow this heat to reach the underside of sea ice. In the Canada Basin, between the cold upper layer and the warm Atlantic layer, a layer of temperature maximum forms another source of heat close to the sea ice, supplied by the intrusion of relatively fresh Pacific waters [*Toole et al*., 2010]. In the Eurasian Basin, the presence of the vertical salinity gradient below the polar mixed layer (the cold halocline layer) restricts the vertical mixing of oceanic heat [*Fer*, 2009, 2014]. In the Fram Strait gateway, along the warm boundary currents, and over topographic features, on the other hand, the turbulent ocean fluxes are elevated by 1 or 2 orders of magnitude [*Lenn et al*., 2009; *Sirevaag and Fer*, 2009; *Shaw and Stanton*, 2014]. The interplay between the vertical mixing processes, advection, ice drift, ice thermodynamics, and the subsequent evolution of the temperature and salinity structure in the upper ocean affect the oceanic heat flux reaching the ice undersurface.

The cold halocline layer in the Eurasian Basin is a perennial feature limiting vertical mixing. Thus, an important question is how much the different processes (e.g., brine rejection in winter, meltwater input in summer, and erosion through turbulent mixing at the base of the mixed layer) contribute to the maintenance of upper ocean stratification in the Arctic. Studies using one-dimensional (1-D) models including vertical turbulent processes to investigate the Arctic ocean halocline and upper ocean stratification have been insightful in this regard [*Davis et al*., 2016; *Ivanov et al*., 2016]. Evaluating the estimated contribution of various terms contributing to the heat budget for the upper ocean, *Polyakov et al*. [2013] concluded that their observations from drifting buoys away from boundary currents were dominated by vertical turbulent processes.

Direct observations of microstructure in winter are sparse in the Arctic Ocean, primarily because of logistical challenges. Notable studies reporting turbulence measurements and turbulent heat fluxes under Arctic sea ice in winter (December–March) are from the SHEBA drift [*Shaw et al*., 2009] and from the drift of an ice-tethered profiler, equipped with a velocity sensor capable of resolving turbulent fluctuations [*Cole et al*., 2014]. Both drifts were in the Beaufort Sea; hence, such winter observations have not been reported from the Eurasian Basin. If we include early spring (April), valuable microstructure observations were made between 2007 and 2014 from the drifting ice camps close to the North Pole [*Fer*, 2009, 2014; *Guthrie et al*., 2015], as well as from drifts north of Svalbard [*Padman and Dillon*, 1991; *Sirevaag and Fer*, 2009]. In situ data acquired during the "Norwegian young sea ICE" (N-ICE2015) campaign [*Granskog et al*., 2016] from January to July 2015, under a wide variety of forcing conditions make a valuable contribution to our present understanding of the ocean-ice-atmosphere system in the Atlantic sector of the Arctic Ocean, north of Svalbard. Here we present observations from a subset of the N-ICE2015 data, collected in winter (February–March 2015), in the Nansen Basin and close to the northern tip of Yermak Plateau.

The N-ICE2015 special section gathers a collection of papers from the experiment covering atmosphere physics, cryosphere, marine biology, and physical oceanography. For a general description of the oceanographic and current conditions see *Meyer et al*., [2017], the microstructure observations and vertical mixing in the water column (upper 300 m) are described in A. Meyer et al. (Mixing rates and vertical heat fluxes north of Svalbard from Arctic winter to spring, submitted to *Journal of Geophysical Research*, 2016), and the under-ice boundary layer turbulence measurements (1 m below the ice) are described in *Peterson et al*. [2017]. These studies present the observations from the entire duration of the experiment, including four different drift floes. Oceanic heat fluxes measured 1 m below the sea ice in the Nansen Basin were $O(1)$ W m^{-2} in winter, and increased by a factor of 2 during wind events [*Peterson et al*., 2017]. The drift in spring was confined to the Yermak Plateau and its slopes, where the combination of wind forcing with shallow Atlantic Water (AW) layer and proximity to open waters lead to rapid melting and large heat fluxes exceeding several 100 W m^{-2} [*Peterson et al*., 2017]. The microstructure observations in the water column were consistent with the findings from the under-ice boundary layer. Winter heat flux across the pycnocline in the Nansen Basin averaged to 3 W m^{-2} during calm conditions and increased significantly to 5 W m^{-2} with storms (A. Meyer et al., submitted manuscript, 2016). Steep topography enhanced dissipation rates by a factor 4 along the eastern slopes of the Yermak Plateau, and episodically increased the turbulent heat flux deeper in the water column. The hydrography was characterized by a strong pycnocline and deep (up to 100 m) mixed layer in winter over the Nansen Basin and the Yermak Plateau slopes. In the late spring, the mixed layer was shallow (less than 20 m deep) over the Yermak Plateau. The AW inflow north of Svalbard was found to be steered by topography, partly along the Svalbard coast and partly around the Yermak Plateau [*Meyer et al*., 2017]. Winter conditions were further sampled in detail using IAOOS platforms; see, e.g., *Koenig et al*. [2016] for hydrographic conditions and *Provost et al*. [2017] for evolution of snow and ice conditions using ice mass balance buoys. *Provost et al*. [2017] report intense sea-ice basal melt in midwinter over warm AW, and snow-ice formation following storms and/or basal ice melt.

In this paper we use winter data from the drift of Floe 1 and 2, to describe the evolution of the hydrography in the upper 200 m by one-dimensional processes, forced by idealized, time-dependent vertical diffusivity profiles inferred from microstructure measurements. We concentrate on the Nansen Basin and exclude effects of advection or proximity to warm AW. The motivation is that simple numerical modeling supplemented by basic information of wind forcing can be used to describe the vertical distribution of upper ocean hydrography from a measured initial state, using representative vertical diffusivity profiles for calm, moderate, and strong wind conditions. Once the dominant 1-D (vertical) processes are identified, our measurements will be useful in the context of the basin-wide seasonal cycle of the mixed-layer heat and freshwater content. Our results, however, are specific to the upper ocean hydrography and vertical mixing processes north of Svalbard, and general conclusions cannot be drawn before further justification of the results for other regions of the Arctic Ocean. Nevertheless, the findings will help better understand the under-studied wintertime entrainment of heat, salinity, and biogeochemical tracers, such as nutrients and oxygen, from deeper water, and are relevant in the broader context of large-scale circulation and tracer studies.

2. Methods

Using the Research Vessel Lance, an experiment was staged north of Svalbard (Figure 1) when four drift stations were occupied between January and June 2015. A brief description of the experiment with aims and motivation is given in *Granskog et al.* [2016]. We use measurements from the period 25 January to 14 March 2015, including 25 days of under-ice eddy-covariance measurements and 45 sets (124 casts) of microstructure profiling.

Data from two instruments are utilized: a vertical microstructure profiler (MSS) and a turbulence instrument cluster (TIC). In the following, details for each type of data collection and reduction are briefly summarized. For further details see A. Meyer et al. (submitted manuscript, 2016) and *Peterson et al.* [2017]. Data sets are available from *Meyer et al.* [2017] and *Peterson et al.* [2016]. Ancillary data used comprise the location of the vessel, 10 min averaged wind measurements from time series combining the on-ice weather station data and the data from ship's mast [*Hudson et al.*, 2015; L. Cohen et al., Meteorological conditions in a thinner Arctic sea ice regime from winter through summer during the Norwegian young sea ICE expedition (N-ICE2015), submitted to *Journal of Geophysical Research*, 2016], and ice thickness survey and ice-coring (profile of ice temperature) conducted by the ice physics group [*Rösel et al.*, 2016; *Gerland et al.*, 2017]. The ship-based wind sensor, mounted at 24 m height, was used to reconstruct gaps in the 10 m wind data from the on-ice weather mast, using the wind profile power law and an empirically derived power that depends on atmospheric stability, calculated as a function of wind speed measured at 24 m (L. Cohen et al., submitted manuscript, 2016). The ice drift velocity is inferred from the ship's GPS position. Instantaneous drift velocity, calculated from first differencing in time of the ship's position, includes inertial and tidal oscillations. Because the upper water column typically oscillates approximately in phase with the ice, the instantaneous drift is not representative of the shear contribution to turbulence production. Therefore, following *McPhee* [2008, Chap. 2.5], we use complex demodulation of daily segments to express the drift velocity as the sum of a mean part (used in our analysis) and oscillations from a combination of clockwise and counterclockwise rotating diurnal and semidiurnal (approximately inertial) components. The instantaneous and filtered drift speeds are shown in Figure 2.

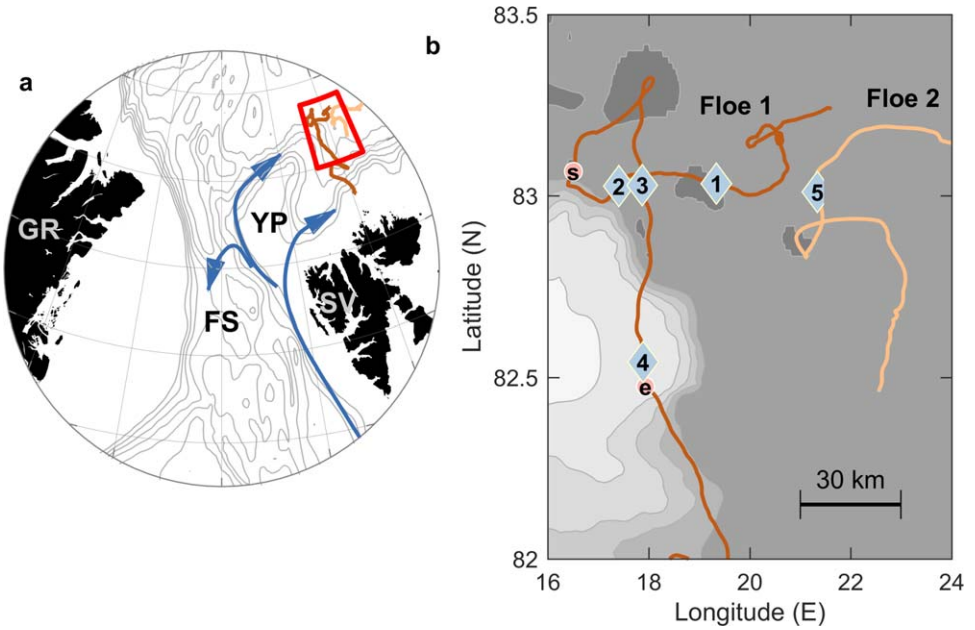

Figure 1. Location map and N-ICE2015 winter drift tracks. (a) The site in relation to Svalbard (SV), Greenland (GR), Fram Strait (FS), and Yermak Plateau (YP). The region marked in red is expanded in Figure 1b. Arrows show the main branches of warm Atlantic Water. Isobaths are drawn at 500 m intervals between 1000 and 6000 m using the 2 min global relief data (ETOPO). (b) Expanded view of the drift tracks (Floe 1, dark brown, and Floe 2 light brown) together with the microstructure locations (sets 1–5, diamonds), and the start and end location of the storm M2 (bullets with s and e). Isobaths are at 500 m intervals from 1 min ETOPO [*Amante and Eakins*, 2009].

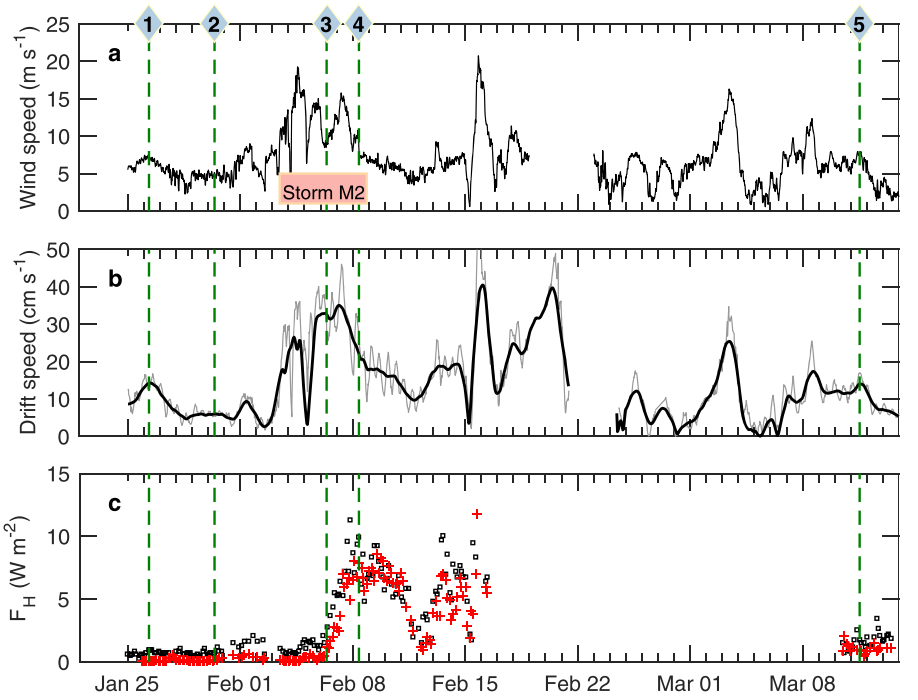

Figure 2. Conditions throughout the study period. Time series of (a) hourly-smoothed, 10 min averaged 10 m wind speed using merged ship-mast (adjusted from 24 m height to 10 m using the wind profile power law detailed in L. Cohen et al. (submitted manuscript, 2016)) and on-ice weather mast data, (b) instantaneous (gray) and filtered, background (black) ice drift speed after complex demodulation using diurnal and semidiurnal frequencies, and (c) turbulent ocean heat flux, F_H. Vertical dashed lines mark the times of microstructure sets 1–5 indicated on top. The storm period (M2) is highlighted in Figure 2a. No data are shown when the ship was repositioning in late February. Heat flux measurements are 3 h averages of 15 min covariances (black circles) and using a bulk parameterization (red).

2.1. Eddy-Covariance Measurements

Under-ice turbulence measurements were made using a TIC deployed 1 m below the ice undersurface. Detailed description of the setup is given by *Peterson et al.* [2017]. High-resolution time series measurements of 3-D velocity components and temperature are collected resolving the energy spectrum from energy containing eddies through the inertial subrange of turbulence. Calculations are based on 15 min segments over which the current components are rotated into the mean current direction (u), such that time averages of the cross-stream (v) and vertical (w) components vanish. The data set is systematically quality controlled before calculating momentum and turbulent heat fluxes (for details see *Peterson et al.* [2017]). Friction velocity at the measurement level is obtained from $u_*=[\langle u'w'\rangle^2+\langle v'w'\rangle^2]^{1/4}$, where primes denote deviation from the mean, and angle brackets denote temporal (15 min) averaging. Temperature measurements in the same measurement volume (2 cm^3) are used to calculate the vertical heat flux, $F_H=\rho c_p\langle w'T'\rangle$, where ρ is the density and c_p is the specific heat capacity of seawater. An alternative estimate of heat flux is obtained for each 15 min segment using a common parameterization dependent on temperature elevation above freezing and friction velocity as $F_{H,bulk}=\rho c_p \mathrm{St}\ u_*(T-T_f)$, where St = 0.0057 is the turbulent Stanton number [*McPhee*, 1992].

The subset of data used here comprises 2407 fifteen minute segments between 25 January and 14 March 2015, which were reduced to 1926 segments after quality control, corresponding to a total duration of approximately 20 days.

2.2. Microstructure Profiling

Vertical profiles of shear microstructure were obtained using an MSS90L profiler equipped with airfoil shear probes. Dissipation rate of turbulent kinetic energy (TKE) is calculated by integrating the vertical wave number spectrum of shear from each probe [*Lueck et al.*, 2002]. Estimates from each probe are corrected for the unresolved variance and a final value is obtained by averaging over the two probes. The processing methods are similar to earlier studies by our group [*Fer*, 2006, 2014] and are summarized in A. Meyer et al.

Table 1. Overview of Microstructure Profile Set Details

Set	Start Date (2015)	Start Time (UTC)	Lon (E)	Lat (N)	Duration (min)	Number of Casts
1	26 Jan	0828	19°20.2′	83°2.0′	45	4
2	30 Jan	0930	17°24.4′	83°1.6′	17	2
3	6 Feb	0847	17°52.2′	83°1.8′	9	3
4	8 Feb	0910	17°53.1′	82°32.6′	25	3
5	11 Mar	1300	21°20.1′	83°0.6′	25	2

(submitted manuscript, 2016). We use 1 m vertically averaged precision temperature and salinity profiles and vertical eddy diffusivity (K) profiles from this data set. The Conservative Temperature, Θ, and Absolute Salinity, S_A, are calculated using the thermodynamic equation of seawater [*IOC, SCOR, IAPSO*, 2010]. K is calculated using the *Osborn* [1980] model as $K=0.2\varepsilon N^{-2}$, assuming the common value of mixing efficiency. For well-mixed layers where N^2 approaches zero, the model is not applicable because it would lead to spuriously large values of K.

In the following analysis a subset of the microstructure profiles is used. The selected profiles are restricted to a region that justifies our assumption of vertical mixing by one-dimensional processes and exclude those affected by advection and proximity to AW. The idealized diffusivity profiles are constructed from 33 out of 45 sets (section 4.3). For numerical solutions, we concentrate on two pairs of profiles, each pair defining the initial and final profile to initiate and compare with the model result, respectively, for two cases separated by 7 days (sets 2 and 3) and 44 days (sets 1 and 5). Another profile (set 4) is used to emphasize the possible effects of advection or other 3-D processes. The details of the five sets of microstructure profiles used here are summarized in Table 1. Motivation for these choices is further given in section 3. Each set is an average profile over two to four casts conducted in a short duration of 10–45 min.

2.3. Salt and Enthalpy Budget at the Ice-Ocean Interface

The numerical solutions of the 1-D diffusion equations described in section 4 require external source terms for temperature and salinity at the upper boundary (ice-ocean interface). These source terms are obtained from the turbulent heat and salinity fluxes calculated from the enthalpy and salt balance at the ice-ocean interface in the under-ice boundary layer. A detailed description can be found in *McPhee* [2008, Chap. 6] and see also *McPhee et al*. [2008]. Here we summarize the sets of equations utilized in characterizing the ocean-ice interaction. The turbulent heat and salinity fluxes at the interface can be written in kinematic form as

$$\langle w'T'\rangle_0=\alpha_H u_{*0}(T_w-T_0), \tag{1}$$

$$\langle w'S'\rangle_0=\alpha_s u_{*0}(S_w-S_0), \tag{2}$$

where α_H and α_s are the turbulent exchange coefficients for heat and salt, respectively, and subscripts 0 and w indicate interface ($z=0$) and far-field seawater (typically in the mixed layer) values. The ratio, $R=\alpha_H/\alpha_s$, of the turbulent exchange coefficients is a measure of strength of heat transfer relative to the salt transfer, and hence of double diffusion. Note that the measurement level of 1 m is usually in the constant stress layer, such that friction velocity is representative of the ice-ocean interface stress. The interface friction velocity can also be approximated from the Rossby similarity drag relation [*McPhee*, 2008], when direct measurements are not available or representative of the drifting ice floe.

Isostatically balanced ice melt rate is $w_0=-(\rho_i/\rho)\dot{h}$, positive upward (melting conditions) where $\dot{h}$ is the ice growth rate (rate of change of ice thickness, positive for growing ice), ρ_i is ice density, and ρ is seawater density. The interface enthalpy conservation strikes a balance between conduction near the bottommost part of the ice, turbulent heat flux from the ocean, and latent heat from melting or freezing. In kinematic form (i.e., energy divided by ρ and specific heat capacity, c_p)

$$\langle w'T'\rangle_0-\dot{q}=w_0Q_L, \tag{3}$$

where the kinematic ice conduction is $\dot{q}=-\frac{k_i}{\rho c_p}\frac{dT_i}{dz}$; $Q_L=L_i/c_p$, and latent heat of fusion for sea ice, L_i, and thermal conductivity of sea ice, k_i, are both obtained from corrections to the fresh ice parameters [see *McPhee*, 2008]. The vertical gradient of ice temperature, $\frac{dT_i}{dz}$, close to the ice undersurface is the driver for conduction through the ice in the considered control volume.

The salt budget leads to a balance between the turbulent salinity flux from the ocean and the net vertical advection of salinity from ice melt or freeze

$$\langle w'S' \rangle_0 + w_0(S_i - S_0) = 0. \tag{4}$$

At the interface, it is often assumed that the salinity is determined by the freezing point temperature, e.g., $T_0 = T_f(S_0) = -mS_0$, with $m = 0.0549$. Finally, combining this set of equations, the so-called "three-equation approach" for the under-ice boundary layer leads to a quadratic equation for the interface salinity, S_0

$$mS_0^2 + aS_0 + b = 0, \tag{5}$$

with

$$a = T_w - \frac{\dot{q}}{\alpha_H u_{*0}} + \frac{Q_L}{R} - mS_i,$$

$$b = -S_i\left(T_w - \frac{\dot{q}}{\alpha_H u_{*0}}\right) - \frac{S_w Q_L}{R}.$$

In this study we use the three-equation approach to calculate the interface heat and salt fluxes at each time step of the numerical solutions and introduce these fluxes as source (or sink) terms into the diffusion equations (6), uniformly distributed over the mixed-layer depth. In summary (see also section 4.2), for prescribed values of S_i, dT_i/dz, R, α_H, u_{*0}, and mixed-layer temperature and salinity, we obtain the interface salinity S_0 from equation (5), and the interface temperature as the corresponding freezing point value. The interface heat flux follows from equation (1). Using the basal melt rate from equation (3), we finally obtain the salt flux at the interface from equation (4).

3. Observations

The period selected for analysis starts with calm conditions, weak winds of approximately 5 m s^{-1} and relatively slow ice drift velocity of about 0.05 m s^{-1}, persisting for 1 week duration, before the storm M2 picks up (Figure 2). We follow the definitions and characterizations of the N-ICE2015 experiment's storms provided by L. Cohen et al. (submitted manuscript, 2016). Start and end of storms correspond to periods when the 10 min averaged wind speed (at 10 m) was greater than 8 m s^{-1} continuously for at least 1 h in a time period of at least 3 h. A major storm (such as M2) is when the rate of pressure decrease exceeds 5 hPa in 6 h. Prior to the storm, oceanic heat fluxes in the under-ice boundary layer are close to the instrument lowest detection level and generally less than 1 W m^{-2} (Figure 2c). After 2.5 days into the storm, the oceanic fluxes start to increase gradually, reaching a peak value of 11 W m^{-2} 4.4 days after the storm starts, and remain large (>5 W m^{-2}) for approximately 2.5 days after the storm ceases. Heat fluxes return to low levels and then increase abruptly when the floe drifts over warm AW after February 11. The average value representative for the "high flux" period is 7 W m^{-2}, calculated between 2 and 11 February. The heat flux measurements from Floe 2 are limited, with 247 fifteen minutes segments between 10 and 14 March (approximately 2.5 days), which have an average heat flux of 2 W m^{-2}.

Wintertime heat fluxes observed here can be compared to available heat flux estimates from previous Arctic studies. In the Canada Basin, *Cole et al*. [2014] report time averaged (October 2009 to April 2010, ± one standard deviation) heat flux of 1.0 (±2.9) W m^{-2} based on covariance measurements at 6 m below ice. During the SHEBA drift in the Beaufort Gyre, average winter under-ice surface heat flux was 1.0 W m^{-2} [*Shaw et al*., 2009]. Estimates using bulk parameterizations ($F_{H,bulk}$ described in section 2.1) were reported using data from drifting buoys. *Krishfield and Perovich* [2005] conclude that $F_{H,bulk}$ is not negligible in winter, but averages less than 2 W m^{-2} in the Beaufort Gyre and is approximately 3 W m^{-2} in the Transpolar Drift. *Jackson et al*. [2012] report that through winter, the average mixed-layer temperature is often marginally above the freezing temperature, leading to typical heat fluxes of the order 1.0 W m^{-2}. Storms during winter, however, result in events with heat flux of 10–50 W m^{-2}, primarily as the release of heat from the near surface temperature maximum (NSTM), which delays the sea ice growth and episodically melts sea ice during winter [*Jackson et al*., 2012]. These high flux events are comparable to, but larger than the average value in our high flux period, probably because of the lack of a NSTM in our study region.

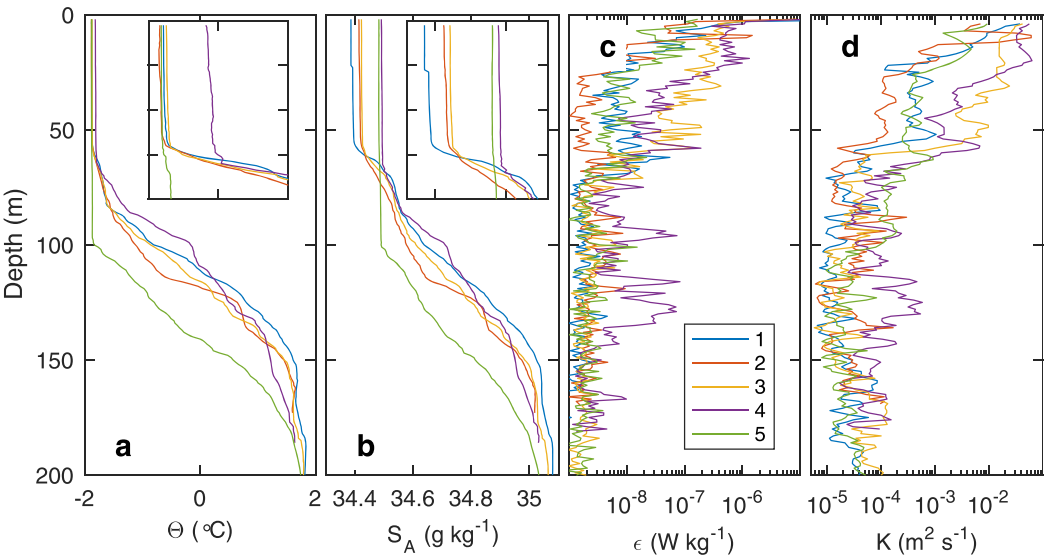

Figure 3. Vertical profiles from sets 1 to 5, measured by the microstructure profiler. Each profile is an average over several casts in the set (see Table 1). Missing values of K in weakly stratified segments are linearly interpolated. Insets are enlarged views in the upper 80 m, with ticks 20 m in the vertical and 0.1°C or 0.1 g kg^{-1} in the horizontal.

In the analysis period, the microstructure profile sets 1–5 (Figure 2 and Table 1) are chosen for discussion. These sets correspond to sets number 2, 5, 11, 12, and 37 of the cruise log. The choice of the sets is motivated by our goal to restrict the analysis to regions where the oceanic response can be attributed to vertical mixing through 1-D processes, forced by wind and affected by surface buoyancy fluxes induced by melting or freezing. Profiles of temperature, salinity, dissipation rates, and eddy diffusivity for sets 1–5 are shown in Figure 3. Sets 1 and 5, separated only by 30 km but 44 days in time, are located in the deep Nansen Basin, unaffected by the presence of AW branch or topography. Sets 1 and 2, on the other hand, are affected by the presence of a front or advection since the substantial increase of salinity in the upper 100 m (Figure 3, insets) in this short time span cannot be explained by vertical processes alone (see sections 5 and 6). Sets 2 and 3, however, are approximately colocated, separated by 1 week duration, with no influence of advection apparent in the temperature and salinity profiles. The profiles of temperature and salinity from sets 3 and 4 show a striking evolution during the storm and swift-drift period where the Absolute Salinity in the mixed layer increases by 0.07 g kg^{-1}, and Conservative Temperature by 0.06°C in two days. Strong vertical mixing during storm leads to rapid and substantial entrainment of warm and saline waters into the mixed layer; however, the increase in Θ and S_A in the mixed layer cannot be explained without including frontal or advection processes. Sets 2 and 3 and sets 1 and 5, on the contrary, are colocated and away from AW influence or fronts; hence, we can study the change in the heat content and salinity using 1-D mixing and entrainment of AW from below.

As further confirmation of the 1-D balance and that mixed-layer temperature and salinity changes are largely due to vertical entrainment, we calculate the change in Θ and S_A averaged between the ice-ocean interface and the $\sigma_\theta = 27.75$ density surface (typically located between 100 and 135 m), between pairs of sets. The choice of a deep isopycnal integrates the effects of mixing at the base of the mixed layer. Because mixing results in a redistribution of water properties vertically, as opposed to a net change, small changes in Θ and S_A indicate dominantly vertical processes whereas relatively large values imply important effect of advection and other processes. For sets 1–5 and 2–3 (used for the 1-D numerical solutions), the change in Θ and S_A is less than 10^{-3} °C d^{-1} or 10^{-3} g kg^{-1} d^{-1}, whereas these values increase by a factor of 5–10 for sets 1–2 and sets 3–4.

In section 5, we first present the evolution from set 2 to 3, a period spanning from calm conditions to 3 days into the storm M2. Next, we concentrate on set 1 to 5 in the Nansen Basin, reproducing the vertical structure of set 5 using 1-D processes, after 44 days of forcing applied to the initial profile, set 1.

4. One-Dimensional Solutions

4.1. Diffusion Equations

We formulate and obtain the solutions for the hydrography in terms of potential temperature, θ, and salinity, S, to be consistent with ice thermodynamics calculations. The solutions are then converted to S_A and Θ for presentation and comparison with observations. One-dimensional diffusion equations for θ and S are

$$\frac{\partial \theta}{\partial t} = \frac{\partial}{\partial z}\left(K\frac{\partial \theta}{\partial z}\right) + S^{\theta},$$
$$\frac{\partial S}{\partial t} = \frac{\partial}{\partial z}\left(K\frac{\partial S}{\partial z}\right) + S^{S}, \tag{6}$$

where all variables, including vertical diffusivity, K, are functions of time, t, and depth (vertical distance from ice, positive upward), and $S^{\theta,\ S}(t,z)$ are the external sources (or sinks) for temperature and salinity (e.g., as a result of heat lost to ice melt or salinity release by freezing, calculated from the ice thermodynamics and described in detail in section 4.2). Solutions are obtained starting from given initial profiles of θ and S, using 1 m vertical and 1 h temporal resolution. At the upper boundary, we apply zero flux (ice-ocean fluxes of heat and salt are distributed over the mixed layer via the source terms, see section 4.2), and at the lower boundary, the bottommost $(\theta,\ S)$ value from the previous time step. Solutions at the final time step of the duration of interest are compared to the observed profiles (the time evolution is not presented). Final profiles are not sensitive to a factor of 2 change to time step or vertical resolution; further sensitivity to different parameter choices is discussed in section 6. Calculations of the source terms and the prescribed K profiles are described in the subsequent subsections.

4.2. Calculations of the Source Terms

The source terms are obtained from the ice thermodynamics, using the interface heat and salt fluxes from the three-equation approach (section 2.3). Temperature gradient in the lowest part of the ice is assigned using temperature profiles from ice core measurements (Figure 4). While there are differences in ice temperature profiles from different floes, the vertical gradient in the bottommost 25 cm is similar, and a line fit to data from three cores yields $dT_i/dz = -5$ K m^{-1}. We assume ice salinity $S_i = 7$ and use the typical temperature near the bottom of ice cores of $T_i = -2.1$°C. We use $R = 33$ and $\alpha_H = 1.3 \times 10^{-2}$ inferred from direct flux measurements in March north of Svalbard [*Sirevaag*, 2009], which are likely representative of the conditions studied here (sensitivity results are given in section 6). The friction velocity, u_{*0}, is obtained from

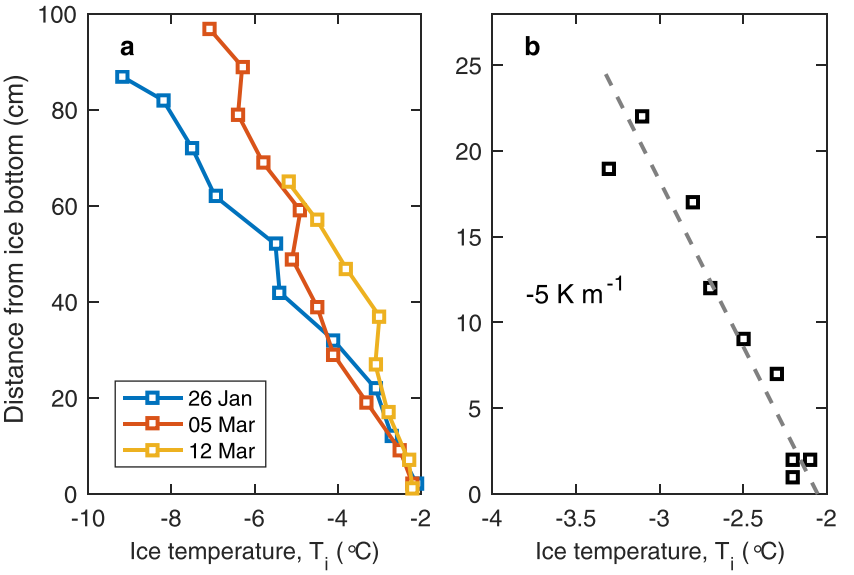

Figure 4. Profiles of ice temperature obtained from ice cores [*Gerland et al.*, 2017]. (a) Entire profile with distance referenced to ice bottom, and (b) zoom in to the bottommost 25 cm together with a least squares fit to a first order polynomial. The slope indicates the estimated ice temperature vertical gradient close to the ice-ocean interface.

the Rossby similarity using the filtered drift speed (removing diurnal and inertial variability) and common values of $A = 1.91$, $B = 2.12$, and $z_0 = 10^{-2}$ m [*McPhee*, 2008]. We do not use the friction velocity measured by the TIC because there is a large gap in the covariance data set between 16 February and 10 March, and also because the floes drift over waters and regions where processes other than vertical mixing can be important, which will have signature on the covariance measurements. By using Rossby similarity and the filtered drift speed, we obtain a more representative forcing for the basin conditions. Using calculations from periods when both estimates are available, average (± one standard deviation) value over daily, half-overlapping windows is 0.007 (±0.004) m s^{-1} for the Rossby similarity and 0.005 (±0.002) m s^{-1}, for the covariance calculations.

Given dT_i/dz, R, α_H, u_{*0}, $m = 0.0549$, and the far-field (at 10 m, in the mixed layer) temperature and salinity, we obtain the interface salinity, S_0, from equation (5). Interface temperature is the corresponding freezing point value, and the interface heat flux follows from equation (1). The basal melt rate, w_0, is then calculated from equation (3) and the salt flux at the interface from equation (4). The resulting interface heat and salt fluxes at each time step are introduced as source (or sink) terms into the diffusion equations (6), uniformly distributed over the mixed-layer depth. For example, during freezing conditions the interface salt flux is a source of salinity to the mixed layer, whereas a positive heat flux (upward across the ice-ocean interface) is a sink for the temperature in the mixed layer. The depth of the mixed layer (z_{ML}) is obtained as the depth where the salinity exceeds the top 2 m average value by 0.1 g kg^{-1}. This method is very similar to the definition from *Peralta-Ferriz and Woodgate* [2015] who used a threshold criterion of potential density of 0.1 kg m^{-3} (for the mixed-layer salinity and temperature values in this study, the salinity excess of 0.1 g kg^{-1} corresponds to approximately 0.08 kg m^{-3}). Increasing and reducing the threshold by 0.05 g kg^{-1}, respectively, leads to 9 m deeper and 5 m shallower z_{ML}, on average. The heat sink term obtained from this calculation is taken up by the ice for melting. This is only a fraction of the oceanic heat delivered to the surface and is accounted for as described in section 4.4.

4.3. Idealized Diffusivity Profiles

We construct idealized profiles of K, from the microstructure measurements collected in the vicinity of sets 1–5, and exclude locations where topography, proximity to AW, and ice edge can affect the vertical mixing (A. Meyer et al., submitted manuscript, 2016a). The stations used are marked in the inset of Figure 5. We use

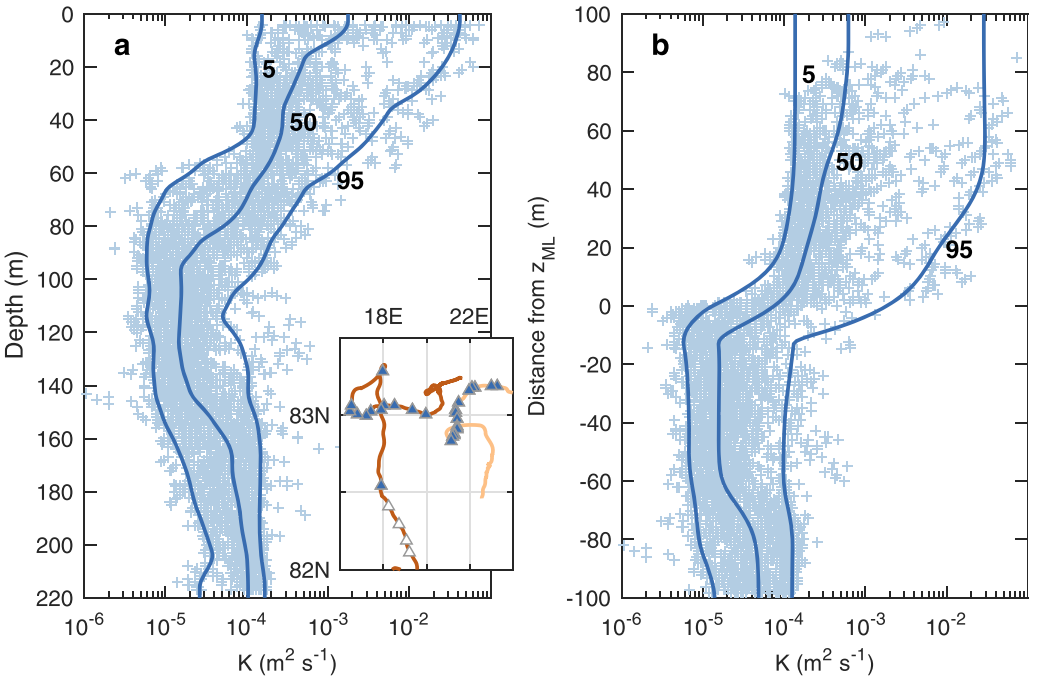

Figure 5. Idealized eddy diffusivity profiles with vertical axis referenced to (a) depth (relative to underside of ice) and (b) distance relative to the base of the mixed layer. Positive values are upward, increasing toward the underside of ice. The profiles from Figure 5b are used in the numerical solutions. All data points from set-averaged profiles (each set includes two to five subsequent casts) are shown (crosses) together with the 5, 50, and 95 percentiles in 10 m thick vertical bins (thick lines). The inset shows a zoom in to the drifts of Floes 1 and 2, all microstructure set positions (white triangles) and the sets used in deriving the idealized profiles (blue triangles).

33 sets out of the 45 collected between 25 January and 14 March 2015: 12 sets (43 casts) from Floe 1, and 21 sets (49 casts) from Floe 2. All K measurements from these sets are shown in the profiles of Figure 5a together with 5, 50, and 95 percentiles in 10 m vertical bins. The vertical diffusivity averaged vertically down to the base of the mixed layer correlates with wind stress, hence u_{*0} (correlation coefficient between wind and $\log_{10}(K)$ is $r = 0.66$, with 34 data points). We therefore can use wind forcing to assign K profiles selectively averaged to be representative of weak, normal, and strong forcing conditions. We use thresholds 5 and 15 m s^{-1} to delineate weak (less than 5 m s^{-1}) and strong wind (greater than 15 m s^{-1}) conditions, approximately corresponding to the 5 and 95 percentiles between 25 January and 14 March 2015. The weak, moderate, and strong wind conditions are represented by the diffusivity profiles K_5, K_{50}, and K_{95}, respectively. The sensitivity to K is presented in section 6. At every hour, the wind speed averaged over the preceding 12 h is used to pick the K profile. The friction velocity is the time average of hourly values over the same 12 h window. The friction velocity used is consistent with the subinertial Rossby similarity approach because we used filtered (demodulated using 24 and 12 h period) drift velocity. The time average is preferable to the instantaneous wind speed and u_{*0}, given the idealized nature of the forcing, and that the K profile should be representative of the temporal history of wind forcing.

The depth of the mixed layer (z_{ML}) varies, and the vertical reach of elevated mixing should be accounted for in assigning time-variable K profiles. We therefore reference the vertical distance to the depth of the mixed layer ($z_r = z_{ML} - z$, positive upward) for each profile and calculate K_5, K_{50}, and K_{95} in 10 m thick bins. Bins with less than 25 data points are excluded. The resulting profiles are then interpolated to 1 m vertical resolution (of z_r) and smoothed over 5 points. One-dimensional solutions are obtained by using these profiles, after mapping z_r onto the actual depth, using the mixed-layer depth from the previous time step.

4.4. Other Details

In order to be consistent with ice thermodynamics calculations, the initial S_A and Θ profiles are converted to salinity in practical scale and potential temperature, and converted back to Absolute Salinity and Conservative Temperature after solving the diffusion equations, in order to compare with the final profiles of set 3 or 5 as applicable.

A positive interface heat flux obtained from the calculations described above is the amount required by ice melt at the ice-ocean interface. The heat sink in the mixed layer can be larger, particularly if additional sensible heat is lost to atmosphere, through the ice or through leads. Thin sea ice and open water cause vigorous surface fluxes compared to the drift station in complete pack ice, in winter leading to increased salt flux into ocean and sensible heat loss to the atmosphere [*Maykut*, 1982]. *Maykut and McPhee* [1995], using data from the AIDJEX experiment, show that heat extracted from the ocean varies largely (35%) between stations separated by 100–200 km, with the main source of variability attributed to the amount of opening by dynamic activity of the sea ice. Only a fraction ϕ of the mixed-layer heat content is thus lost to ice melt. Over a homogeneous ice field (i.e., excluding the heat loss through openings and leads), *Rudels et al*. [1999] suggested a natural control mechanism whereby ϕ is optimized to keep the ice melt rate at a minimum. Using the temperature difference between upper layer and the warm layer below, ΔT, and the salinity of the warm layer, S_w, the fraction of heat going to ice melt is

$$\phi = \frac{2\alpha L}{c_p(\beta S_w - \alpha \Delta T)}, \tag{7}$$

where α and β are the thermal expansion and haline contraction coefficients of seawater, respectively, and L is the latent heat of melting. For $S_w = 34.9$ and $\Delta T = 3°C$, ϕ is approximately 0.16. In the calculations, at each time step, the heat sink is multiplied by $1/\phi$. The salinity source term is applicable only when there is ice freezing and convection. For these conditions, we assume convection occurs over a fraction, F, of the representative area and multiply the salinity source term by a factor of $F = 0.6$ (chosen because of better agreement with observations; sensitivity is discussed in section 6).

The imposed fractions ϕ and F lead to a mixed layer that cools more and freshens less than what ice-ocean heat and salt fluxes would prescribe. This adjustment, however, is crucial because (i) the upper ocean heat content is not controlled by the heat loss to ice melt alone, but also includes a part that is lost to the atmosphere, and (ii) neither heat loss nor convection occurs homogenously over an area representative of the study site. Leads in the pack ice allow rapid ice formation and escape of oceanic heat to the atmosphere.

During the study period, leads opened up sporadically and quickly refroze (P. Itkin et al., Thin ice and storms: A case study of sea ice deformation from buoy arrays deployed during N-ICE2015, submitted to *Journal of Geophysical Research*, 2016), such that we deem their contribution to regulating surface heat and salt fluxes crucial.

5. Results

Over the 1 week that separates sets 2 and 3, the mixed-layer depth remained approximately constant at 58–60 m, the mixed-layer averaged temperature increased by 0.01°C, and salinity by 0.007 g kg^{-1}. The vertical profiles of Θ and S_A are compared to the numerical solution after 7 days in Figure 6 (compare orange and red curves). The evolution can be explained by vertical processes dependent on our choice of parameters and the sensitivity discussed in section 6. The evolution between sets 1 and 5 over 44 days are more striking (Figure 7). Mixed-layer depth increased from 56 to 100 m, and the pycnocline deepened by approximately 20 m. Mixed-layer salinity has increased by 0.094 g kg^{-1} while temperature increased by 0.002°C, staying close to freezing. In both cases, the changes in the mixed layer are well replicated by the one-dimensional model. A shortcoming of the numerical solution is the lack of a vertical convective adjustment scheme to ensure a sharp mixed-layer base. The vertical diffusivity leads to a diffuse transition from the mixed layer to the pycnocline; the temperature and salinity characteristics in the upper half of the mixed layer, however, are in very good agreement with the observations. The discrepancy between the observed and modeled depth of the pycnocline can be considered to be within the short-term variability such as internal waves.

A direct comparison with a snapshot observed profile suffers from not sufficiently averaging over internal wave displacements and other short-term variability. In order to account for the vertical heave inherent in the observations, in Figures 6 and 7 we destrain the observed profiles by linearly stretching or squashing the vertical coordinate to maintain the $\sigma_\theta = 27.75$ density surface at a fixed depth (of the initial profile, 105 m for set 1 and 117 m for set 2). This isopycnal is chosen to be close to z_{ML} but away from the effects of mixing at the base of the mixed layer. This procedure assumes that internal wave and eddy displacements are zero at the surface and increase linearly with depth below—a reasonable approximation in the upper water column. Destraining results in upward displacements of −7 and −2 m in the final profile of observation and model, respectively, for the 7 day run, and 25 and 13 m for the 44 day run. In the figures we also indicate a typical vertical displacement of the pycnocline of ±10 m for reference. This is 3–5 times less than

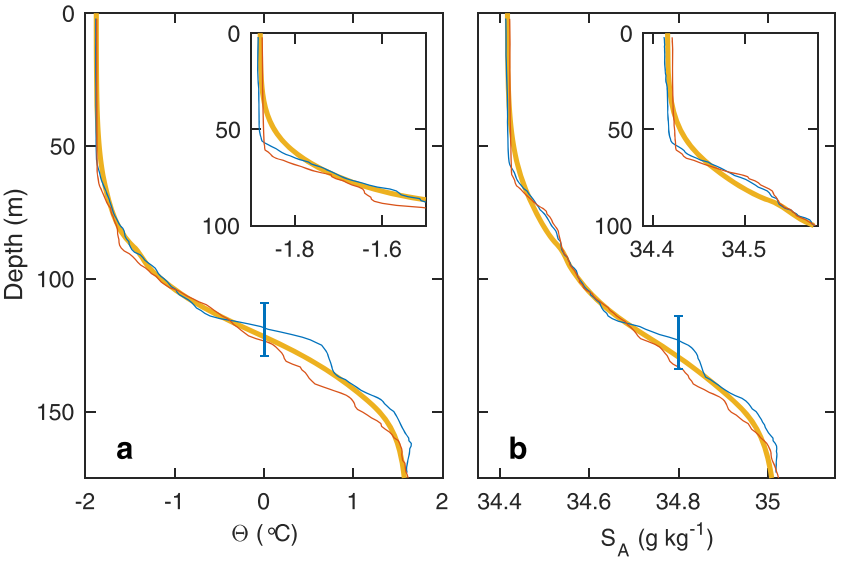

Figure 6. Vertical profiles of (a) Conservative Temperature and (b) Absolute Salinity for set 2 (initial condition, 30 January, blue), set 3 (6 February, red), and the solution obtained from the time-dependent diffusion equations over the time separation of approximately 7 days (thick orange curve). The insets zoom in to the upper 100 m. The vertical error bar is placed arbitrarily to indicate, for reference, a typical ± 10 m vertical displacement of temperature and salinity surfaces from internal waves. The vertical axis is the depth for the initial profile, but destrained (see text) depth for the final profiles.

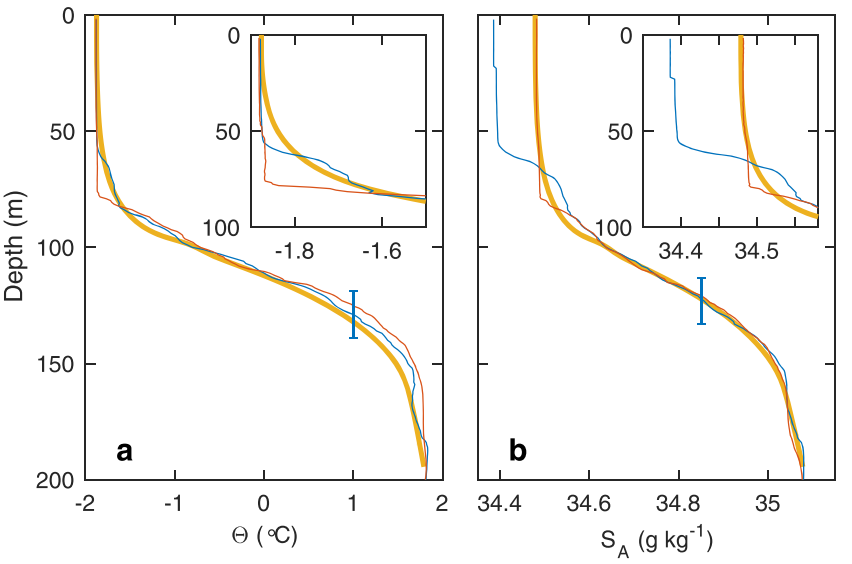

Figure 7. Same as Figure 6 but for set 1 (blue) and 5 (red). Time separation is approximately 44 days.

the vertical displacements observed in the upper 200 m over the southern Yermak Plateau [*Fer et al.*, 2010], and can be considered as a representative value for the study area. In the Canada Basin, typical vertical displacements are smaller: Using ice-tethered profiler data for years 2005–2014, *Dosser and Rainville* [2016] obtain typical wave amplitudes (for near-inertial waves below the mixed layer, in the upper 200 m) that decrease from approximately 2 m to less than 1 m between 72°N and 82°N latitude.

Over the 44 day simulation period, vertical mixing was forced 15% of the time by weak wind (K_5 profile) and 7% of the time strong wind (K_{95} profile) conditions. Main results for this experiment are summarized in Table 2. Salinity increase in the mixed layer was 0.1 g kg^{-1} (very close to the observed value); 10% of this is attributed to increase from brine release during freezing, calculated from the salinity source term. Because we do not apply convective adjustment, but simply distribute the salinity source throughout the mixed layer, the remaining 90% can be attributed to entrainment from beneath the mixed layer. Freezing conditions ($w_0 < 0$) occurred 70% of the time. Over the freezing periods, w_0 averaged to -1.2 (± 0.5) 10^{-8} m s^{-1}, or -0.10 (± 0.05) cm d^{-1}. This can be compared to the total (ice and snow) thickness growth estimates from transects on Floes 1 and 2 (Figure 8). The observed ice and snow thickness growth rate (not identical to w_0) is 3–4 times larger. This is not conclusive as the discrepancy can be accounted for, for example, by an increase in snow thickness, but suggests that the model produces growth rates of the right order. Melting conditions occurred in response to strong entrainment events during strong wind forcing, in four abrupt episodes, two events during storm M2, and between 15 and 16 February and 3 and 4 March. Averaged over melting periods, w_0 was 0.3 (± 0.2) cm d^{-1}. Salinity increase in the mixed layer due to entrainment from below during these episodes accounted for 70% of the total increase (Table 2).

Table 2. Overview of Results From the 44 Day Run[a]

	Total	Freezing Periods	Melting Periods
Duration (day)	44	70%	30%
w_0 (cm d^{-1})		−0.1	0.3
$\Delta\Theta$ (°C)		40%	60%
0–25 m	0.005		
0-z_{ML}	0.090		
ΔS_A (g kg^{-1})		30%[b]	70%
0–25 m	0.092		
0-z_{ML}	0.100		

[a]Total increase in the Conservative Temperature and Absolute Salinity relative to the initial profile, averaged over the upper 25 m or over the mixed-layer depth, z_{ML}, over the total duration are listed together with corresponding percent increase over the freezing and melting periods only. The percent of time with freezing and melting conditions, and the corresponding average basal melt rates, w_0, are also given.

[b]Of the 30%, 10% is due to brine release (from the source term) and 90% from entrainment because of vertical mixing.

As a consequence of the diffuse mixed-layer base, the lower part of the mixed layer shows a signature of elevated entrainment of heat and salt compared to

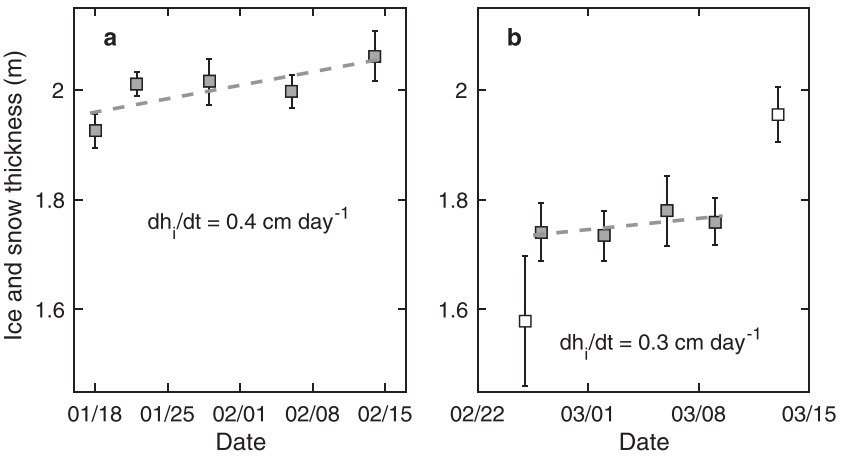

Figure 8. Total ice thickness (ice plus snow) growth rate estimates from electromagnetic induction sounding transects [*Rösel et al.*, 2016] on (a) Floe 1 and (b) Floe 2. Only subsets of floe data relevant to this study are used (e.g., Floe 1 excludes the part when drifting over Atlantic Water and transects over first year ice). Data points are the median values of typically 1000 measurements obtained from one transect. Error bars are standard errors assuming (arbitrarily) every 100th data point is independent. Linear least squares fits are shown together with the slope. The open markers in Figure 8b are excluded from the fit because those surveys include various types of ice and are not representative of the standard repeat transect.

the observations. Averaged over the mixed layer, temperature increase is 0.09°C, much larger than the observed 0.002°C, primarily due to the increase in the lower part of the mixed layer. When averaged only in the uppermost 25 m, the temperature increase is 0.005°C, much closer to the observations. The corresponding figure for salinity is 0.092 g kg^{-1}, in excellent agreement with observations (0.094 g kg^{-1}), and only slightly lower than the full mixed-layer depth average of 0.1 g kg^{-1} from the model. This suggests that the effect of diffuse mixed-layer base does not influence salinity as much as it does temperature, which is probably explained by the under-ice boundary layer temperature kept at freezing point. This constraint maintains a large mixed layer to pycnocline temperature difference. On the other hand, the relatively saline pycnocline water is entrained and redistributed into the mixed layer, reducing the mixed layer to pycnocline salinity difference relative to the initial state, leading to a thinner diffuse salinity layer.

6. Sensitivity

The calculations using the simplified model are based on choices of several parameters that deserve a sensitivity analysis. The aim of the additional calculations presented here with altered values of selected parameters is not to assess the upper ocean response to perturbations (such as freshening, increased forcing, etc.), but to identify how sensitive our results and findings are to a large (factor of 2–10) change on the choices made. The parameters can be grouped in relation to ice-ocean interface and thermodynamics (ice temperature gradient, heat exchange coefficient, and double diffusion strength), forcing (wind and vertical diffusivity), and fractions relating to leads and openings. Wind speed does not come directly into the analysis, but is used as a proxy for the vertical diffusivity chosen to be dependent on the wind speed. We therefore present detailed cases of sensitivity to vertical diffusivity.

The double diffusion strength imposed by R does not lead to notable changes in the mixed-layer temperature and salinity properties (Figure 9). The results however are sensitive to the heat exchange coefficient: a reduction of α_H by a factor of 2 leads to warmer temperatures by 0.028°C (averaged in the upper 50 m); while this does not affect the salinity, doubling of α_H leads to slightly higher (0.005 g kg^{-1}) salinity. Overall, the choices of α_H and R thus do not affect our results significantly.

Vertical diffusivity, on the other hand, changes the vertical structure significantly. We tested idealized profiles of K (time dependent, chosen using the same wind speed thresholds), multiplied by a factor of 5 and by a factor of 0.2, for the entire water column, as well as a factor of 5 increase only in the mixed layer (5 × K-ML in Figure 10). Additionally, we obtained solutions for time-constant K prescribed by the moderate K_{50} profile, independent of the wind speed. The results are summarized in Figure 10. Strong vertical mixing leads to substantial deepening of the mixed layer and entrainment into the mixed layer, exceeding the

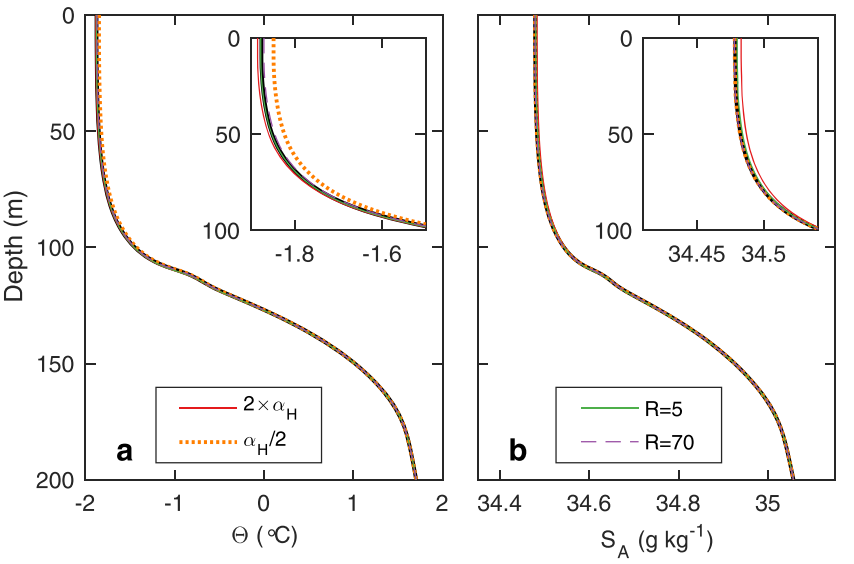

Figure 9. Sensitivity to parameters α_H and R. Profiles of (a) Conservative Temperature and (b) Absolute Salinity are shown. Black line, not included in the legend, is the reference solution shown in Figure 7. The legends are valid for all panels. The axis limits are the same for Figures 9–11 but note that the limit of the salinity inset is different than in Figure 7.

observed values by a large factor, particularly for salinity estimates (see Figure 10b, light green trace off scale in the inset). Entrainment is less when only the mixed layer K is increased; however, the final profile is still inconsistent with the observations. The constant K_{50} profile results in a shallower mixed layer compared to the observations (or to the reference solution in black which captures the observations fairly well). The sensitivity analysis implies that the time variable, wind-dependent K forcing is needed to faithfully capture the evolution in the upper water column.

Finally, the sensitivity of the results to the prescribed temperature gradient in the lower part of ice, and to the choices of fractions ϕ and F, is examined (Figure 11). Compared to the role played by vertical diffusivity, the effect of these parameters in the salinity profile is small, but slightly more important than the effect of α_H and R. When brine rejection is allowed in the entire surface area ($F = 1$), the salinity in the mixed layer is

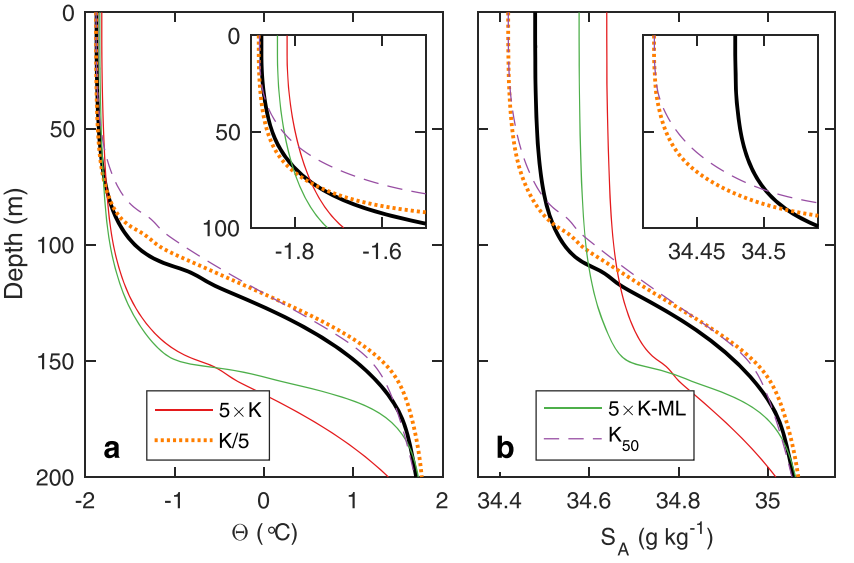

Figure 10. Same as Figure 9 but for sensitivity to vertical diffusivity. Solutions are obtained for 5 and 1/5 times the reference K profile, which is time variable and dependent on the wind speed, and for the reference K profile increased by a factor of 5 in the mixed layer only (5×K-ML). Additionally the solution is presented for a constant diffusivity profile equal to K_{50}.

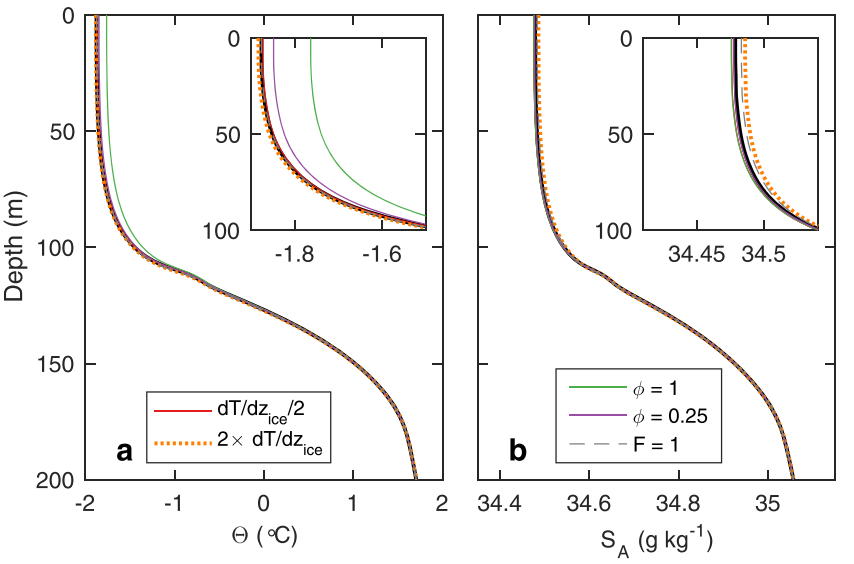

Figure 11. Same as Figure 9 but for sensitivity to ice temperature gradient, fraction ϕ, and the area fraction *F*.

0.005 g kg^{-1} larger. Doubling of the ice temperature gradient leads to even higher salinities (Figure 11, increase of 0.007 g kg^{-1} from the reference case). Of the parameters related to thermodynamics, double diffusion and area fractions, the fraction ϕ controls the mixed-layer temperatures. This is induced through control on the heat source term. When all of the heat available is allowed to melt sea ice ($\phi = 1$), temperature in the mixed layer is warmer by more than 0.1°C.

7. Discussion

Three essential features evolve from set 1 to 5: Salinity in the mixed layer increases, the mixed layer deepens, and the upper halocline freshens (Figure 7). Set 5 was located further away from the Yermak Plateau and from the influence of AW, compared to set 1. We therefore expect set 5 to be affected by certain trends: First, AW is expected to lie deeper at set 5, and second, winter mixed layers become increasingly deeper as one moves away from the immediate margins of the Eurasian Basin [*Meyer et al.*, 2017]. However, the increased influence of less saline Arctic water masses away from the basin margins would imply a relatively fresh mixed layer; the opposite is clearly the case, and this feature can thus not be explained as a consequence of spatial variation.

Our 1-D modeling captures all of these three features. We are thus confident that the majority of the change from set 1 to 5 is temporal. The rather small dependence of the model results on ice-ocean interaction related parameters further indicates that the bulk of the time evolution stems from diapycnal mixing in the water column. In fact, brine rejection from freezing ice accounts for only 10% of the mixed-layer salinity increase. The entrainment into the mixed layer is dominated by winter storms (>15 m/s; see Figure 2) rather than by buoyancy fluxes at the ice-ocean interface. A similar observation was made in the cold wake of a hurricane where most of the sea surface temperature change was due to entrainment by vertical mixing rather than air-sea heat fluxes [*D'Asaro et al.*, 2007].

The simple model applied here can be compared to more physically and dynamically based (e.g., on gradient Richardson number based mixing) models such as the Price-Weller-Pinkel [*Price et al.*, 1986] model with superimposed thermodynamics sea ice layer applied to summer and winter cases in the central Canada Basin [*Toole et al.*, 2010], or the local turbulence closure scheme of *McPhee* [1999]. The ability of the simple one-dimensional model to describe the observed evolution of the upper water column supports the hypothesis that in Arctic basins away from the ice edge, warm boundary currents and significant freshwater input, vertical processes are primarily responsible for shaping the temperature and salinity distribution, rather than lateral movement of water masses. Lateral mixed-layer restratification processes were observed to

be active in the Canada Basin [*Toole et al*., 2010], e.g., due to eddies in the upper water column [*Timmermans et al*., 2008], which cannot be captured by any of the one-dimensional models. Since observations reported here were made in winter, freshwater from sea ice melt is not considered. In spring and summer, however, freshwater increases stratification in the surface layer, which inhibits mixing. During melting conditions, the influence of double diffusion increases, significantly reducing the ocean-to-ice heat flux [*McPhee et al*., 1987; *Sirevaag*, 2009]. Our sensitivity results, however, do not show substantial changes in the mixed-layer temperature and salinity for a wide range of R and a factor of 2 change of the heat exchange coefficient.

In the Eurasian Basin, the perennial pycnocline is a bottleneck for the mixing of tracers between the mixed layer and the underlying warm and nutrient-rich AW. Thus in the Atlantic sector of the Arctic Ocean, nutrient fluxes are subject to similar dynamics as heat fluxes, and we can expect similar patterns for the vertical nutrient flux and the heat flux. Our results give indications on how much halocline water was entrained into the mixed layer between sets 1 and 5. As *Randelhoff and Guthrie* [2016] noted, in the Atlantic inflow area to the Arctic ocean, nitrate concentration is mixed conservatively with density over the relevant depth range; the same holds for nitrate concentration as a function of salinity. Regression of nitrate concentration against Absolute Salinity determined from a CTD bottle cast on 26 January, the same day the microstructure set 1 was sampled, shows excellent correlation ($R^2 = 0.99$, S_A range between 34.4 and 35.1, nitrate concentration range between 4 and 15 μM, variance of residual is 0.2 μM^2). Our results on entrainment of salinity and heat are directly applicable to entrainment of nitrate without further consideration of possibly not colocated pycnoclines and nutriclines as is the case, e.g., in the Canadian Basin. We can thus argue for a correlation between the upward flux of nutrients and the mixed-layer salinity increase due to entrainment during the same period.

The large mixed layer deepening from 60 to 100 m between set 1 and 5, and entrainment were dominated by the few winter storms which lead to upper pycnocline dissipation rates far above the usually rather quiescent values observed in the Arctic Ocean [*Fer*, 2009, 2014]. *Polyakov et al*. [2013] estimate an annual average upward heat flux of 1 W m^{-2} from the upper pycnocline in the central Eurasian Basin, and contrast this with a January–April average of 3–4 W m^{-2}. This corroborates a substantial seasonal cycle in entrainment of Atlantic Water. Similarly, enhanced vertical mixing (from storms and convection) through fall and winter has been shown to be a major driver in the seasonal replenishment of upper ocean heat and nutrient inventories [*Nishino et al*., 2015; *Randelhoff et al*., 2015, 2016]. *Randelhoff and Guthrie* [2016] report back-of-the-envelope calculations of convective entrainment of nitrate assuming that the wintertime brine rejection balances summertime sea ice melt. Our results indicate that wind-driven entrainment (as opposed to brine rejection induced, convective entrainment) can in fact contribute significantly to the annual mixed-layer density budget. For the N-ICE2015 study area, this has two implications. First, the convection driven entrainment is presumably even smaller than that given by *Randelhoff and Guthrie* [2016]. Second, upper halocline waters have to be renewed either through a convective-advective mechanism [*Rudels et al*., 1996] to achieve an interannual steady state, or by upward diffusion of deeper halocline waters during summer when surface meltwater restricts vertical mixing to above upper halocline waters [*Randelhoff et al*., 2017].

8. Concluding Remarks

A one-dimensional model is presented to describe the evolution of the hydrography in the upper 200 m in the Atlantic sector of the Arctic Ocean, in the Nansen Basin north of Svalbard. The model is forced by idealized, time-dependent vertical diffusivity profiles inferred from microstructure measurements. Two pairs of stations are examined, separated by 7 and 44 days in time, respectively, when the effects of advection and lateral processes were negligible. The model reproduces the observed changes well for both sets. The deepening of the pycnocline over 44 days is qualitatively captured by the model; however, the base of the mixed layer is diffuse compared to the observed profiles. The changes observed in the two pairs of stations in the Nansen Basin are dominated by vertical mixing processes. The sensitivity analysis implies that the time variable, wind-dependent forcing is needed to faithfully capture the evolution in the upper water column.

For the studied period between 26 January and 11 March 2015, 10% of the salinity increase in the mixed layer is attributed to increase from brine release during freezing which occurred 70% of the time, whereas the remaining 90% can be attributed to entrainment from beneath the mixed layer. Melting conditions occurred

in response to entrainment events during episodic strong wind forcing. Salinity increase in the mixed layer during these episodes accounted for 70% of the total increase. We conclude that the increase in salinity as a result of freezing is significantly less than that due to entrainment (approximately 10% versus 90%), and the latter is affected by episodic wind events (70% versus 30%). The study is specific to the upper ocean hydrography and vertical mixing processes north of Svalbard, and general conclusions cannot be drawn; nevertheless, the findings have implications for wintertime entrainment of temperature, salinity, and biogeochemical tracers from deeper water, and are relevant in the broader context of large-scale circulation and tracer studies.

Acknowledgments

The field work and A.M. have been supported by the Norwegian Polar Institute's Centre for Ice, Climate and Ecosystems (ICE) through the N-ICE project. A.K.P. is supported by the Research Council of Norway, through the project 229786. Additional support was obtained from the Centre for Climate Dynamics at the Bjerknes Centre through the BASIC project. A.R. was supported through CARBON BRIDGE (project 226415) funded by the Norwegian Research Council. We thank Miles McPhee for making the TIC instrumentation available, the ice physics group for making the ice core and EM data available, and the atmospheric forcing group for making the wind data available. We thank the captains, crews, and sciences parties for their help in making this study possible. Comments from two reviewers helped improve the manuscript substantially. Data used in this study are publicly available at the Norwegian Polar Data Centre: MSS data [*Meyer et al*., 2016], TIC data [*Peterson et al*., 2016], surface meteorology data [*Hudson et al*., 2015], ice core data [*Gerland et al*., 2017], and EM31 total (snow and ice) thickness data [*Rösel et al*., 2016].

References

Amante, C., and B. W. Eakins (2009), ETOPO1 1 arc-minute global relief model: Procedures, data sources and analysis, *NOAA Tech. Memo. NESDIS NGDC-24*, Natl. Geophys. Data Cent., NOAA, USA, doi:10.7289/V5C8276M.

Carmack, E., et al. (2015), Towards quantifying the increasing role of oceanic heat in sea ice loss in the new Arctic, *Bull. Am. Meteorol. Soc.*, *96*, 2079–2105, doi:10.1175/BAMS-D-13-00177.1.

Cole, S. T., M.-L. Timmermans, J. M. Toole, R. A. Krishfield, and F. T. Thwaites (2014), Ekman veering, internal waves, and turbulence observed under Arctic Sea Ice, *J. Phys. Oceanogr.*, *44*, 1306–1328, doi:10.1175/JPO-D-12-0191.1.

D'Asaro, E. A., T. B. Sanford, P. P. Niiler, and E. J. Terrill (2007), Cold wake of Hurricane Frances, *Geophys. Res. Lett.*, *34*, L15609, doi:10.1029/2007GL030160.

Davis, P. E. D., C. Lique, H. L. Johnson, and J. D. Guthrie (2016), Competing effects of elevated vertical mixing and increased freshwater input on the stratification and sea ice cover in a changing Arctic Ocean, *J. Phys. Oceanogr.*, *46*, 1531–1553, doi:10.1175/Jpo-D-15-0174.1.

Dosser, H. V., and L. Rainville (2016), Dynamics of the changing near-inertial internal wave field in the Arctic Ocean, *J. Phys. Oceanogr.*, *46*, 395–415, doi:10.1175/jpo-d-15-0056.1.

Fer, I. (2006), Scaling turbulent dissipation in an Arctic fjord, *Deep Sea Res., Part II*, *53*, 77–95.

Fer, I. (2009), Weak vertical diffusion allows maintenance of cold halocline in the central Arctic, *Atmos. Oceanic Sci. Lett.*, *2*, 148–152.

Fer, I. (2014), Near-inertial mixing in the Central Arctic Ocean, *J. Phys. Oceanogr.*, *44*, 2031–2049, doi:10.1175/JPO-D-13-0133.1.

Fer, I., R. Skogseth, and F. Geyer (2010), Internal waves and mixing in the Marginal Ice Zone near the Yermak Plateau, *J. Phys. Oceanogr.*, *40*, 1613–1630.

Gerland, S., M. A. Granskog, J. King, and A. Rösel (2017), *N-ICE2015 Ice Core Physics: Temperature, Salinity and Density*, Norw. Polar Inst., Norway, doi:10.21334/npolar.2017.c3db82e3.

Granskog, M. A., P. Assmy, S. Gerland, G. Spreen, H. Steen, and L. H. Smedsrud (2016), Arctic research on thin ice: Consequences of Arctic sea ice loss, *Eos*, *97*, 22–26, doi:10.1029/2016EO044097.

Guthrie, J. D., I. Fer, and J. H. Morison (2015), Observational validation of the diffusive convection flux laws in the Amundsen Basin, Arctic Ocean, *J. Geophys. Res. Oceans*, *120*, 7880–7896, doi:10.1002/2015JC010884.

Hudson, S. R., L. Cohen, and V. P. Walden (2015), N-ICE2015 Surface Meteorology, Norw. Polar Inst., Norway, doi:10.21334/npolar.2015.056a61d1.

IOC, SCOR, IAPSO (2010), The international thermodynamic equation of seawater - 2010: Calculations and use of thermodynamic properties, in *Manuals and Guides No. 56*, Intergov. Oceanogr. Comm., UNESCO, France.

Ivanov, V., V. Alexeev, N. V. Koldunov, I. Repina, A. B. Sando, L. H. Smedsrud, and A. Smirnov (2016), Arctic Ocean heat impact on regional ice decay: A suggested positive feedback, *J. Phys. Oceanogr.*, *46*, 1437–1456, doi:10.1175/Jpo-D-15-0144.1.

Jackson, J. M., W. J. Williams, and E. C. Carmack (2012), Winter sea-ice melt in the Canada Basin, Arctic Ocean, *Geophys. Res. Lett.*, *39*, L03603, doi:10.1029/2011GL050219.

Koenig, Z., C. Provost, N. Vilacieros-Robineau, N. Sennéchael, and A. Meyer (2016), Winter ocean-ice interactions under thin sea ice observed by IAOOS platforms during N-ICE2015: Salty surface mixed layer and active basal melt, *J. Geophys. Res. Oceans*, *121*, 7898–7916, doi:10.1002/2016JC012195.

Krishfield, R. A., and D. K. Perovich (2005), Spatial and temporal variability of oceanic heat flux to the Arctic ice pack, *J. Geophys. Res.*, *110*, C07021, doi:10.1029/2004JC002293.

Lenn, Y. D., et al. (2009), Vertical mixing at intermediate depths in the Arctic boundary current, *Geophys. Res. Lett.*, *36*, L05601, doi:10.1029/2008GL036792.

Lueck, R. G., F. Wolk, and H. Yamazaki (2002), Oceanic velocity microstructure measurements in the 20th century, *J. Oceanogr.*, *58*, 153–174.

Maykut, G. A. (1982), Large-scale heat exchange and ice production in the central Arctic, *J. Geophys. Res.*, *87*(C10), 7971–7984, doi:10.1029/JC087iC10p07971.

Maykut, G. A., and M. G. McPhee (1995), Solar heating of the Arctic mixed layer, *J. Geophys. Res.*, *100*(C12), 24,691–24,703.

McPhee, M. G. (1992), Turbulent heat flux in the upper ocean under sea ice, *J. Geophys. Res.*, *97*(C4), 5365–5379.

McPhee, M. G. (1999), Parameterization of mixing in the ocean boundary layer, *J. Mar. Syst.*, *21*, 55–65.

McPhee, M. G. (2008), *Air-Ice-Ocean Interaction: Turbulent Ocean Boundary Layer Exchange Processes*, 215 pp., Springer, New York.

McPhee, M. G., G. A. Maykut, and J. H. Morison (1987), Dynamics and thermodynamics of the ice/upper ocean system in the marginal ice zone of the Greenland Sea, *J. Geophys. Res.*, *92*(C7), 7017–7031.

McPhee, M. G., J. H. Morison, and F. Nilsen (2008), Revisiting heat and salt exchange at the ice-ocean interface: Ocean flux and modeling considerations, *J. Geophys. Res.*, *113*, C06014, doi:10.1029/2007JC004383.

Meyer, A., et al. (2016), N-ICE2015 Ocean Microstructure Profiles (MSS90L), Norw. Polar Inst., Norway, doi:10.21334/npolar.2016.774bf6ab.

Meyer, A., et al. (2017), Winter to summer hydrographic and current observations in the Arctic Ocean north of Svalbard, *J. Geophys. Res. Oceans*, doi:10.1002/2016JC012391, in press.

Nishino, S., Y. Kawaguchi, J. Inoue, T. Hirawake, A. Fujiwara, R. Futsuki, J. Onodera, and M. Aoyama (2015), Nutrient supply and biological response to wind-induced mixing, inertial motion, internal waves, and currents in the northern Chukchi Sea, *J. Geophys. Res. Oceans*, *120*, 1975–1992, doi:10.1002/2014JC010407.

Osborn, T. R. (1980), Estimates of the local rate of vertical diffusion from dissipation measurements, *J. Phys. Oceanogr.*, *10*, 83–89.

Padman, L., and T. M. Dillon (1991), Turbulent mixing near the Yermak Plateau during the coordinated Eastern Arctic Experiment, *J. Geophys. Res.*, *96*(C3), 4769–4782.

Peralta-Ferriz, C., and R. A. Woodgate (2015), Seasonal and interannual variability of pan-Arctic surface mixed layer properties from 1979 to 2012 from hydrographic data, and the dominance of stratification for multiyear mixed layer depth shoaling, *Prog. Oceanogr.*, *134*, 19–53, doi:10.1016/j.pocean.2014.12.005.

Peterson, A. K., A. Randelhoff, I. Fer, A. Meyer, L. Håvik, L. H. Smedsrud, I. Onarheim, M. Muijlwick, A. Sundfjord, and M. G. McPhee (2016), N-ICE2015 Ocean Turbulent Fluxes From Under-Ice Turbulent Cluster, Norw. Polar Inst., Norway, doi:10.21334/npolar.2016.ab29f1e2.

Peterson, A. K., I. Fer, M. G. McPhee, and A. Randelhoff (2017), Turbulent heat and momentum fluxes in the upper ocean under Arctic Sea Ice, *J. Geophys. Res. Oceans*, doi:10.1002/2016JC012283, in press.

Polyakov, I. V., A. V. Pnyushkov, R. Rember, L. Padman, E. C. Carmack, and J. M. Jackson (2013), Winter convection transports atlantic water heat to the surface layer in the eastern Arctic Ocean, *J. Phys. Oceanogr.*, *43*, 2142–2155, doi:10.1175/JPO-D-12-0169.1.

Price, J. F., R. A. Weller, and R. Pinkel (1986), Diurnal cycling: Observations and models of the upper ocean response to diurnal heating, cooling, and wind mixing, *J. Geophys. Res.*, *91*(C7), 8411–8427.

Provost, C., N. Sennéchael, J. Miguet, P. Itkin, A. Rösel, Z. Koenig, N. Villacieros-Robineau, and M. A. Granskog (2017), Observations of flooding and snow-ice formation in a thinner Arctic sea ice regime during the N-ICE2015 campaign: Influence of basal ice melt and storms, *J. Geophys. Res. Oceans*, doi:10.1002/2016JC012011, in press.

Randelhoff, A., and J. D. Guthrie (2016), Regional patterns in current and future export production in the central Arctic Ocean quantified from nitrate fluxes, *Geophys. Res. Lett.*, *43*, 8600–8608, doi:10.1002/2016GL070252.

Randelhoff, A., A. Sundfjord, and M. Reigstad (2015), Seasonal variability and fluxes of nitrate in the surface waters over the Arctic shelf slope, *Geophys. Res. Lett.*, *42*, 3442–3449, doi:10.1002/2015GL063655.

Randelhoff, A., I. Fer, A. Sundfjord, J.-É. Tremblay, and M. Reigstad (2016), Vertical fluxes of nitrate in the seasonal nitracline of the Atlantic sector of the Arctic Ocean, *J. Geophys. Res. Oceans*, *121*, 5282–5295, doi:10.1002/2016JC011779.

Randelhoff, A., I. Fer, and A. Sundfjord (2017), Turbulent upper-ocean mixing affected by meltwater layers during Arctic summer, *J. Phys. Oceanogr.*, doi:10.1175/jpo-d-16-0200.1, in press.

Rudels, B. (2015), Arctic Ocean circulation, processes and water masses: A description of observations and ideas with focus on the period prior to the International Polar Year 2007-2009, *Prog. Oceanogr.*, *132*, 22–67, doi:10.1016/j.pocean.2013.11.006.

Rudels, B., L. G. Anderson, and E. P. Jones (1996), Formation and evolution of the surface mixed layer and halocline of the Arctic Ocean, *J. Geophys. Res.*, *101*(C4), 8807–8821.

Rudels, B., H. J. Friedrich, D. Hainbucher, and G. Lohmann (1999), On the parameterisation of oceanic sensible heat loss to the atmosphere and to ice in an ice-covered mixed layer in winter, *Deep Sea Res., Part II*, *46*, 1385–1425.

Rösel, A., et al. (2016), N-ICE2015 Total (Snow and Ice) Thickness Data From EM31, Norw. Polar Inst., Norway, doi:10.21334/npolar.2016.70352512.

Shaw, W. J., and T. P. Stanton (2014), Vertical diffusivity of the Western Arctic Ocean halocline, *J. Geophys. Res. Oceans*, *119*, 5017–5038, doi:10.1002/2013JC009598.

Shaw, W. J., T. P. Stanton, M. G. McPhee, J. H. Morison, and D. G. Martinson (2009), Role of the upper ocean in the energy budget of Arctic sea ice during SHEBA, *J. Geophys. Res.*, *114*, C06012, doi:10.1029/2008JC004991.

Sirevaag, A. (2009), Turbulent exchange coefficients for the ice/ocean interface in case of rapid melting, *Geophys. Res. Lett.*, *36*, L04606, doi:10.1029/2008GL036587.

Sirevaag, A., and I. Fer (2009), Early spring oceanic heat fluxes and mixing observed from drift stations north of Svalbard, *J. Phys. Oceanogr.*, *39*, 3049–3069.

Timmermans, M.-L., J. Toole, A. Proshutinsky, R. Krishfield, and A. Plueddemann (2008), Eddies in the Canada Basin, Arctic Ocean, observed from ice-tethered profilers, *J. Phys. Oceanogr.*, *38*, 133–145, doi:10.1175/2007jpo3782.1.

Toole, J. M., M. L. Timmermans, D. K. Perovich, R. A. Krishfield, A. Proshutinsky, and J. A. Richter-Menge (2010), Influences of the ocean surface mixed layer and thermohaline stratification on Arctic Sea ice in the central Canada Basin, *J. Geophys. Res.*, *115*, C10018, doi:10.1029/2009JC005660.